atoms

MDPI

Article

Theoretical Calculation of Ground and Electronically Excited States of $MgRb^+$ and $SrRb^+$ Molecular Ions: Electronic Structure and Prospects of Photo-Association

Mohamed Farjallah [1,2], Hela Ladjimi [2,3], Wissem Zrafi [1,2] and Hamid Berriche [2,4,*]

[1] Electronic Department, Higher Institute of Applied Sciences and Technology of Sousse, University of Sousse, Sousse 4003, Tunisia; farjallah_mohamed@yahoo.fr (M.F.); zrafi_wissem@yahoo.fr (W.Z.)
[2] Laboratory of Interfaces and Advanced Materials LR11ES55, Faculty of Science of Monastir, Physics Department, University of Monastir, Monastir 5019, Tunisia; hela.ladjimi@fuw.edu.pl
[3] Faculty of Physics, University of Warsaw, Pasteura 5, 02-093 Warsaw, Poland
[4] Department of Mathematics and Physics, School of Arts and Sciences, American University of Ras Al Khaimah, Ras Al Khaimah 10021, United Arab Emirates
* Correspondence: hamid.berriche@aurak.ac.ae

Abstract

In this work, a comprehensive theoretical investigation is carried out to explore the electronic and spectroscopic properties of selected diatomic molecular ions $MgRb^+$ and $SrRb^+$. Using high-level ab initio calculations based on a pseudopotential approach, along with large Gaussian basis sets and full valence configuration interaction (FCI), we accurately determine adiabatic potential energy curves, spectroscopic constants, transition dipole moments (TDMs), and permanent electric dipole moments (PDMs). To deepen our understanding of these systems, we calculate radiative lifetimes for vibrational levels in both ground and low-lying excited electronic states. This includes evaluating spontaneous and stimulated emission rates, as well as the effects of blackbody radiation. We also compute Franck–Condon factors and analyze photoassociation processes for both ions. Furthermore, to explore low-energy collisional dynamics, we investigate elastic scattering in the first excited states ($2^1\Sigma^+$) describing the collision between the Ra atom and Mg^+ or Sr^+ ions. Our findings provide detailed insights into the theoretical electronic structure of these molecular ions, paving the way for future experimental studies in the field of cold and ultracold molecular ion physics.

Keywords: ab initio; pseudopotential; configuration interaction; potential energy curves; spectroscopic constants; dipole moment; vibrational levels; elastic collision

check for updates

Academic Editor: Cleanthes A. Nicolaides

Received: 4 May 2025
Revised: 7 July 2025
Accepted: 14 July 2025
Published: 25 July 2025

Citation: Farjallah, M.; Ladjimi, H.; Zrafi, W.; Berriche, H. Theoretical Calculation of Ground and Electronically Excited States of $MgRb^+$ and $SrRb^+$ Molecular Ions: Electronic Structure and Prospects of Photo-Association. *Atoms* **2025**, *13*, 69. https://doi.org/10.3390/atoms13080069

Copyright: © 2025 by the authors. Licensee MDPI, Basel, Switzerland. This article is an open access article distributed under the terms and conditions of the Creative Commons Attribution (CC BY) license (https://creativecommons.org/licenses/by/4.0/).

1. Introduction

Molecular ions formed through the interaction of trapped ions and ultracold atoms have recently attracted considerable attention as a promising candidate for investigating fundamental aspects of quantum-controlled chemistry, cold collision dynamics [1–7]. Their unique long-range interactions and controllable internal degrees of freedom make them highly suitable for a variety of applications. These include high-resolution molecular spectroscopy [2], ultracold collision studies [5–9], quantum computing [10,11], precision measurement [12], quantum simulation [11–15], and investigations into many-body physics [16]. A common experimental setup for ion–atom studies features laser-cooled alkaline-earth-metal ions confined in a Paul trap, overlapped with ultracold alkali-metal

atoms confined in magnetic, magneto-optical, or optical dipole traps [1]. Alkaline-earth-metal ions and alkali-metal atoms are commonly utilized due to their unique electronic configurations, which are particularly well suited for laser cooling applications [17]. In addition, these molecular ions present a special long-range property, describing the interactions between an ion and atom, providing many opportunities for investigating collisional dynamics within the quantum *s*-wave scattering regime [18,19]. Hetero-nuclear molecular ions composed of alkali, alkaline-earth atoms, and their related ions are employed to make ultra-cold molecular ions through magneto-association, photo-association, and the stimulated Raman adiabatic process STIRAP [20–23]. These approaches offer precise control over molecular formation, allowing for the creation of systems in order to explore new areas in quantum science.

Mølhave and Drewsen demonstrated that using laser-cooled atomic cations in a linear Paul trap, alkaline-earth mono-hydrid ions can be produced [24]. Atomic cations are excited by the cooling laser and readily resisted by the gas molecules that are purposefully positioned in the background [25]. Kosloff et al. [26,27] used laser-cooled atomic ions to compute the photo-dissociation of the magnesium hydride cation integrated in Coulomb crystals.

Recent theoretical studies on electronic structure have focused on potential energy curves, permanent and transition dipole moments, as well as static dipole polarizabilities of the electronic states in $AlkEH^+$ molecular systems, where AlkE represents Be, Mg, Ca, Sr, and Ba atoms [28–31]. Core polarization potentials (CPPs) and effective core potential (ECPs) were combined to include valence–core electron correlations. Electronic energies were calculated using the two-electron complete configuration interaction (FCI) approach in all these publications. Tomza et al. [32] have conducted a theoretical investigation of the ground electronic state of single-charged molecular ions that result from the interaction of two or three alkali-metal and alkaline-earth-metal atoms using the CCSD(T) method. The ground-state electronic characteristics of molecular ions containing Li, Na, K, Rb, Cs, Mg, Ca, Sr, Ba, as well as most triatomic A_2B^+ species are also calculated [32].

Several cold atomic ion–atom combinations, such as Ca^++Rb [33], Ca^++Li [34], Ca^++Na [35], and Sr^++Rb [36], have already been the subject of experimental investigations. However, it has been observed that Ca^+Rb [37] and Ba^+Rb [38] molecular ions can form as a result of cold collisions between the respective ions and atoms. In addition, for a long time there has been a constant interest in the electrical structure of alkaline-earth molecular ions, such as $BeAlk^+$, $MgAlk^+$, $CaAlk^+$ $SrAlk^+$, and $BaAlk^+$ (Alk = Li, Na, K, Rb, and Cs) [18,20,22,39–42].

The ground state and several excited states of the molecular ion $SrRb^+$ has previously been investigated and represented by Aymar et al. [21,42]. However, only the ground state has been theoretically predicted for molecular ion $MgRb^+$ and the spectroscopic and structural details of the excited states remain unknown [32].

Using an enhanced ab initio pseudopotential method established by Foucrault et al. [43], along with large Gaussian basis sets and full FCI, we present the results of a theoretical analysis of the low-lying electronic states of $AlkERb^+$ (AlkE = Mg and Sr). The adiabatic potential energy curves for the $^{1,3}\Sigma^+$, $^{1,3}\Pi$, and $^{1,3}\Delta$ symmetries are then found, together with their spectroscopic constants, permanent and transition dipole moments, and a vigorous analysis of these molecular ionic systems is presented.

The structure of this paper is as follows: Section 2 offers a concise overview of the computational methodology and numerical parameters used in this study. Section 3, divided into tree sebsections, devoted to present our findings adiabatic potential energy curves for and their spectroscopic constants for the ground and many excited states of $^{1,3}\Sigma^+$, $^{1,3}\Pi$ symmetries for $MgRb^+$ and $SrRb^+$ diatomic molecular ions, permanent and

transition dipole moments as well as the discussion of the possibility of formation via photoassociation. In Section 4, we finally provide a summary of our findings.

2. Methods of Calculation

$SrRb^+$ and $MgRb^+$ were studied using the semiempirical pseudopotential method in its semi-local form, as proposed by Fuentealba et al. [43]. In this approach, the Mg^{2+}/Sr^{2+} and Rb^+ cores are replaced by effective core potentials (ECPs).

$$V_{ps}^{Sr,M_g} = -\frac{z}{r} + \sum_{l=0} B_l^{Sr,M_g} exp\left(-\beta_l^{Sr,M_g} r^2\right) P_l^{Sr,M_g} \quad (1)$$

where $P_l^{Sr,M_g} = \sum_m |lm\rangle_{Sr,Mg}\langle lm|_{Sr,Mg}$ is the projection operator onto the subspace of angular momentum l, r is the radial distance from the nucleus, z denotes the core charge of the ion (z = 2 for Sr^{2+} or Mg^{2+}), B_l^{Sr,M_g} is an empirical parameter fitted to reproduce atomic energy levels for angular momentum quantum number l (l = 0,1,2 corresponding to s, p, d symmetries, respectively), and β_1 denotes the exponential decay parameter for the Gaussian term associated with l.

The resulting systems are thus treated as two-valence-electron molecules, where the electrons move in the field of the Mg^{2+}/Sr^{2+} and Rb^+ ions. The interactions between the polarizable ionic cores and the valence electrons are described using the core polarization potential (V_{CPP}) formulated by Müller et al. [44].

$$V_{CPP} = -\frac{1}{2}\sum_{\lambda=A,B} \alpha_\lambda \vec{f}_\lambda . \vec{f}_\lambda \quad (2)$$

where A and B denote the Sr/Mg and Rb atoms and α_λ denotes the dipole polarizability of the core λ. The electric field f_λ, generated on λ by valence electrons and other cores, is modified by a cutoff function F, which acts specifically on the electronic contribution:

$$f_\lambda = \sum_{i=1}^{2} \frac{r_{i\lambda}}{r_{i\lambda}^3} F(r_{i\lambda}\rho_\lambda) - \sum_{\lambda\neq\lambda'} \frac{R_{\lambda',\lambda}}{R_{\lambda',\lambda}^3} Z_{\lambda'} \quad (3)$$

where $r_{i,\lambda}$ represents the relative position vector between the i-th valence electron and the core λ, while $R_{\lambda'\lambda}$ denotes the core–core relative positions between cores λ′ and λ. The cutoff function F is expanded as the following form:

$$F(r_{i,\lambda},\rho_\lambda) = \sum_l \sum_{m=-l}^{l} F_l\left(r_{i,\lambda},\rho_\lambda^l\right) |lm\rangle_\lambda \langle lm|_\lambda \quad (4)$$

where $F_l\left(r_{i,\lambda},\rho_\lambda^l\right)$ is defined by the following: $F_l\left(r_{i,\lambda},\rho_\lambda^l\right) = 0\ for\ r_{i,\lambda} < \rho_\lambda^l$.

$$F_l\left(r_{i,\lambda},\rho_\lambda^l\right) = 1\ for\ r_{i,\lambda} \geq \rho_\lambda^l$$

l-dependent cutoff functions $F_l\left(r_{i,\lambda},\rho_\lambda^l\right)$ are introduced because valence electrons interact differently with cores depending on their angular symmetry l, while the $r_{\lambda l}$ parameters have been fitted to reproduce experimental energies [45] averaged over the rotational quantum number J. In the present work, the optimized cutoff parameters for the lowest valence s, p, and d are one-electron states, and the dipole polarizabilities of Sr, Mg, and Rb atoms are represented in Table 1.

After the self-consistent field (SCF) calculation, the full-valence configuration interaction (FCI) is performed using the CIPSI algorithm (Configuration Interaction by Perturba-

tive Selection of Iteratively optimized multiconfigurational wavefunctions), implemented through the standard suite of programs developed by the Laboratoire de Physique Quantique in Toulouse, France. To ensure an accurate representation of the electronic structure for both molecular systems, $MgRb^+$ and $SrRb^+$, we employed extended Gaussian-type basis sets for all atoms involved. For the magnesium atom, we slightly modified the basis set from Ref. [46], expanding it from (8s5p4d2f/7s5p3d2f) to (9s7p5d4f/7s7p4d4f). For the strontium and rubidium atoms, we used (5s5p6d/5s5p3d) and (7s4p5d1f/6s4p4d1f) basis sets, respectively [41,47,48], with diffuse exponents optimized to accurately reproduce the 5s, 5p, 4d, 6s, and 6p atomic states [45].

Table 1. Polarizabilities and cutoff radii parameters for Rb, Mg, and Sr atoms (in a.u.).

	Rb	**Mg**	**Sr**
α	9.245	0.46904	5.51
$r_c(s)$	2.5213	0.900	2.0893
$r_c(p)$	2.279	1.25499	2.1170
$r_c(d)$	2.511	1.500	1.64471
$r_c(f)$	2.511	1.500	1.64471

One possible approach for forming molecular ions in the ground electronic state, as investigated in this study, involves single-photon photoassociation (PA). In this process, a pair of atoms + ions ($Sr^+(^2S)$ + $Rb(^2S)$/$Mg^+(^2S)$ + $Rb(^2S)$) colliding at ultralow energies are initially in the first excited $2^1\Sigma^+$ state. This is followed by spontaneous emission, allowing the system to relax into the ground state $1^1\Sigma^+$, resulting in the formation of $MgRb^+$ or $SrRb^+$ molecular ions. For this objective, we use the interaction potentials calculated above as input data for the short-range potential. The long-range part is given by the following:

$$V_{eff}(r) = -\frac{1}{2}\left(\frac{C_4}{r^4} + \frac{C_6}{r^6}\right) \tag{5}$$

where C_4 and C_6 are related, respectively, to the static dipole and quadrupole polarizabilities of the neutral Rb atom for both the $MgRb^+$ and $SrRb^+$ cases. We use C_4 = 318 a.u and C_6 = 6480 a.u [49]. Using the partial wave decomposition method, the effective potential of the ion–atom system can be written as follows:

$$V_{eff}(r) = -\frac{1}{2}\left(\frac{C_4}{r^4} + \frac{C_6}{r^6}\right) + \frac{\hbar^2}{2\mu r^2}l(l+1) \tag{6}$$

where r is the internuclear separation between atom and ion, μ is the reduced mass of an ion–atom colliding pair, and l is the partial wave of the system. Here, the quantity $\frac{\hbar^2}{2\mu r^2}l(l+1)$ represents the centrifugal energy barrier, which inhibits collisions involving partial waves with $l > 0$ in the low-energy regime.

The time-independent Schrödinger equation for different partial waves can be expressed as follows:

$$\left[\frac{d^2}{dr^2} + k^2 - \frac{2\mu}{r^2}V(r) - \frac{l(l+1)}{r^2}\right]\psi_l(kr) = 0 \tag{7}$$

The asymptotic form of the scattering wave function is given by $\psi_l(kr) \sim \sin\left[kr - \frac{l\pi}{2} + \eta_l\right]$, where η_l is the phase shift for the l-th partial wave, and $k = \frac{\sqrt{2\mu E}}{\hbar}$.

The corresponding differential Equation (2) can be numerically solved using the Numerov method [50]. The total elastic scattering cross section is given by the following:

$$\sigma_{el} = \frac{4\pi}{k^2}\sum_{l=0}^{\infty}(2l+1)sin^2(\eta_l) \tag{8}$$

In the high-energy collision regime, the total cross section of the ion–atom system can be approximated by the following classical expression:

$$\sigma_{tot} \sim \pi\left(\frac{\mu C_4^2}{\hbar^2}\right)\left(1+\frac{\pi^2}{16}\right)E^{-1/3} = C_E E^{-1/3} \tag{9}$$

In addition, the radiative lifetimes of vibrational levels supported by the potential energy curves (PECs) of electronic states can be evaluated using the following expression:

$$\tau_i^{-1} = \sum_{f<i} A_{if} + \sum_f B_{if} \tag{10}$$

In this equation, i and f are the initial and final vibrational levels, respectively. The first term, A_{if}, represents the Einstein coefficient for spontaneous emission from the upper vibrational level i to a lower-level f, and is given by the following:

$$A_{if} = \frac{4\omega_{if}^3}{3C^3}|\langle i|\mu(R)|f\rangle|^2 \tag{11}$$

Here, ω_{if} is the transition frequency between levels i and f, calculated as $\omega_{if} = \left|E_f - E_i\right|$, where E_i and E_f are the energies of the respective vibrational levels. The function $\mu(R)$ is the electronic transition dipole moment, evaluated along the internuclear distance R. The second term in Equation (10), B_{if}, accounts for blackbody radiation (BBR)-induced transitions. It describes both stimulated emission and absorption and is related to A_{if} through the following:

$$B_{if} = A_{if}N\left(\omega_{if}\right) \tag{12}$$

where $N(\omega_{if})$ is the average number of thermal photons at the transition frequency, given by the following:

$$N\left(\omega_{if}\right) = \left(exp\left(\frac{\omega_{if}}{k_B T}\right) - 1\right)^{-1} \tag{13}$$

with B in k_B being the Boltzmann constant and T the temperature.

To determine the radiative lifetimes of vibrational levels in the $A^1\Sigma^+$ electronic state, both bound–bound and bound–free transitions must be considered. The bound–bound contribution to the inverse lifetime is given by the following:

$$\tau_{v'} = \frac{1}{\Gamma_{v'}}; \Gamma_{v'} = \sum_{v=0}^{nvt} A_{vv'} \tag{14}$$

where $A_{vv'}$ is the Einstein coefficient for transitions from vibrational level v' to lower levels v. For bound–free transitions, we apply the Franck–Condon approximation. The corresponding contribution $\boldsymbol{A_{v'}^{cont}}$ is estimated as follows:

$$\boldsymbol{A_{v'}^{cont}} = \frac{64\ \pi^2}{3h^4c^3}|\mu(R_{v'+})|^2 FC_{v',cont}\left(\Delta E_{v',cont}\right)^3 \tag{15}$$

where $\Delta E_{v',cont} = E_{v'} - E_{as}$, with $E_{v'}$ representing the energy of the bound vibrational level and E_{as} the energy of the continuum threshold. The dipole moment $\mu(R_{v'+})$ is evaluated at the classical outer turning point of the v' level.

The continuum Franck–Condon factor is defined as follows:

$$FC_{v',cont} = \int |\langle \chi_{v'} | \chi_E \rangle|^2 dE = 1 \sum_{v=0}^{nvt} |\langle \chi_{v'} | \chi_v \rangle|^2 \quad (16)$$

3. Results and Discussion

3.1. Adiabatic Potential Energy Curves (PECs) and Spectroscopic Constants

In this work, we are interested in the interaction of the Rb atom with the alkaline-earth-metal Mg and Sr atoms and ions in ground and excited electronic states for different molecular electronic states of $^{1,3}\Sigma^+$, $^{1,3}\Pi$, and $^{1,3}\Delta$ symmetries. Table 2 provides a summary of the electronic configurations and terms, along with the corresponding molecular ground and excited states. It also includes the valence energies representing the binding energies of the valence electrons—up to the seventh dissociation limit for the $(MgRb)^+$ and $(SrRb)^+$ molecular ions. The binding energy of valence electrons is defined as the energy difference between the $(Mg+Rb)^+/(Sr+Rb)^+$ atomic threshold, in a specific electronic state with two valence electrons, and the $(Mg+Rb)^{3+}/(Sr+Rb)^{3+}$ configuration, which corresponds to the fully ionized form without any valence electrons from Rb or Mg/Sr. The experimental values are derived from the first and second ionization energies of Mg or Sr, along with the first ionization energy of Rb [48]. The resulting molecular transition energies for both $MgRb^+$ and $SrRb^+$ are reported in Table 2, where they are compared with available experimental data [48] and other theoretical predictions [39,42]. The asymptotic energy levels for both systems are well reproduced.

Table 2. Lowest atomic asymptotes, their experimental (**Exp**) and theoretical (**Theo**) valence energies, and associated molecular electronic states for $MgRb^+$ and $SrRb^+$ molecular ions.

Ion	State	Asymptotic Limit	This Work	Exp [45]	Theo [42]	Theo [39]
$MgRb^+$						
	$\mathbf{X^1\Sigma^+}$	$Mg(^1S(3s^2)) + Rb^+$	0	0		
	$\mathbf{1^3\Sigma^+, 1^3\Pi}$	$Mg(^3P(3s3p)) + Rb^+$	21,875	21,994		
	$\mathbf{2^1\Sigma^+, 2^3\Sigma^+}$	$Mg^+(^2S(3s)) + Rb(^2S(5s))$	27,978	28,116		
	$\mathbf{3^1\Sigma^+, 1^1\Pi}$	$Mg(^1P(3s3p)) + Rb^+$	35,049	35,181		
	$\mathbf{4^1\Sigma^+, 2^1\Pi, 3^3\Sigma^+, 2^3\Pi}$	$Mg^+(^2S(3s)) + Rb(^2P(5p))$	40,715	40,853		
	$\mathbf{4^3\Sigma^+}$	$Mg(^3S(3s4s)) + Rb^+$	41,195	41,154		
	$\mathbf{5^1\Sigma^+}$	$Mg(^1S(3s4s)) + Rb^+$	43,501	43,472		
$SrRb^+$						
	$\mathbf{X^1\Sigma^+}$	$Sr(^1S(5s^2)) + Rb^+$	0	0	0	0
	$\mathbf{2^1\Sigma^+, 1^3\Sigma^+}$	$Sr^+(^2S(5s)) + Rb(^2S(5s))$	12,402	12,147	12,441	-
	$\mathbf{2^3\Sigma^+, 1^3\Pi}$	$Sr(^3P(5s5p)) + Rb^+$	14,965	14,710	14,627	14,548
	$\mathbf{3^3\Sigma^+, 2^3\Pi, 1^3\Delta}$	$Sr(^3D(5s4d)) + Rb^+$	18,722	18,258	18,795	18,242
	$\mathbf{3^1\Sigma^+, 1^1\Pi, 1^1\Delta}$	$Sr(^1D(5s4d)) + Rb^+$	20,893	20,150	20,810	20,209
	$\mathbf{4^1\Sigma^+, 2^1\Pi}$	$Sr(^1P(5s5p)) + Rb^+$	21,480	21,699	21,455	21,459
	$\mathbf{5^1\Sigma^+, 3^1\Pi, 4^3\Sigma^+, 3^3\Pi}$	$Sr^+(^2S(5s)) + Rb(^2P(5p))$	25,139	24,884	-	-

In the case of molecules, the Schrödinger equation is solved for an attributed position of the nuclei (internuclear distance). Each new internuclear distance corresponds to a set of new electronic wave functions and new energies that are always ranked in ascending order. In this work, the PECs for the $AlkERb^+$ systems (where AlkE = Mg or Sr) are computed using the full-valence configuration interaction (FCI) method. Figure 1 shows the adiabatic

PECs corresponding to the seven lowest dissociation limits of different symmetries $^{1,3}\Sigma^+$, $^{1,3}\Pi$, and $^{1,3}\Delta$ for the $MgRb^+$ (panel (a)) and $SrRb^+$ (panel (b)) molecular ions. These PECs have been investigated in the range of internuclear distances from 5 to 80 Bohr for both molecules, with a very small interval around equilibrium positions and avoided crossings. The calculated energies at large distances are compared to theoretical and experimental atomic transition energies as already observed in the description of the molecular excited states of $MgRb^+$ and $SrRb^+$ in Table 2.

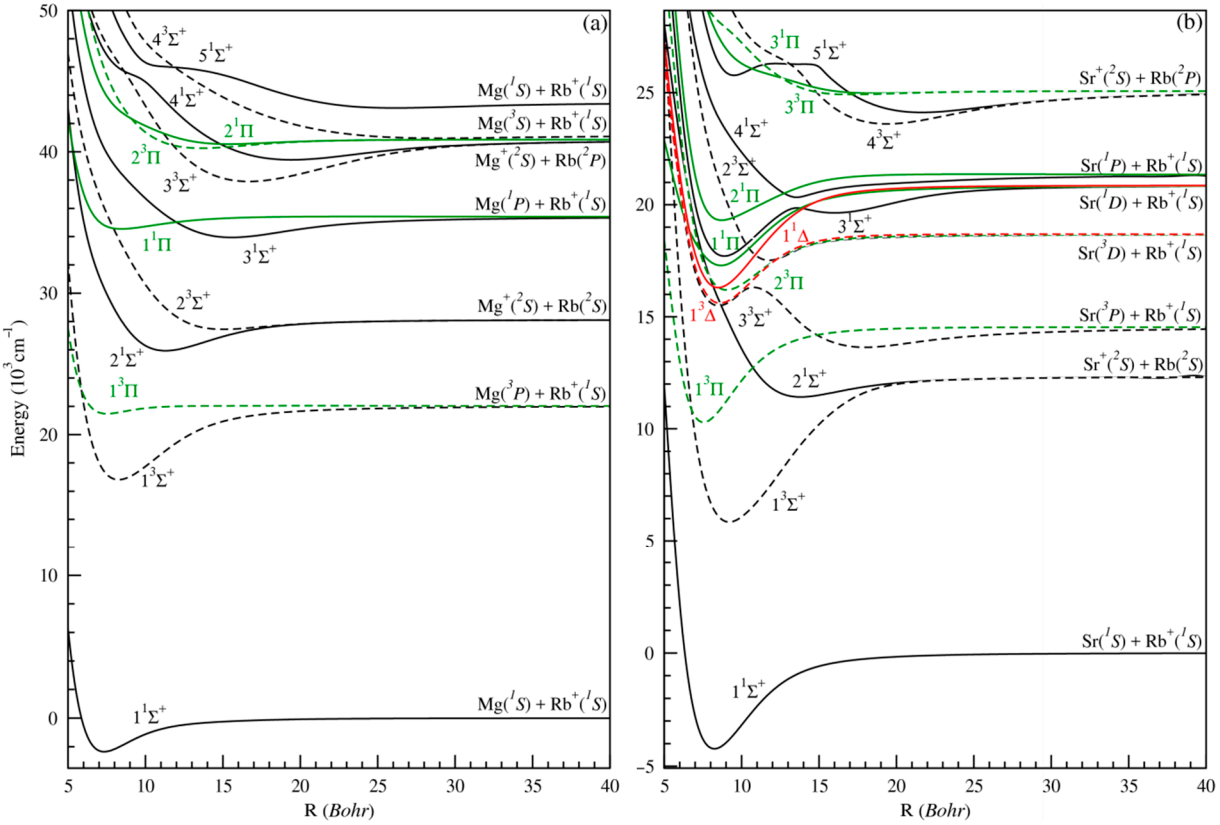


Figure 1. Potential energy curves of the ground and low-lying excited states of $MgRb^+$ (panel (**a**) and $SrRb^+$ (panel (**b**)). Atomic dissociation channels for the states are indicated in the figures (and Table 2).

An initial examination of Figure 1 shows that nearly PECs are smooth and exhibit a clearly defined single minimum, especially for the lowest electronic states. However, several higher-excited states display intriguing features, such as double-well potentials, local maxima (humps), and numerous ionic–neutral avoided crossings. These features occur at both short and long intermolecular distances across various excited states and can largely be attributed to interactions between the electronic states of the $AlkERb^+$ systems (with AlkE = Mg or Sr). Such avoided crossings are particularly significant, as they can greatly influence excitation and charge transfer efficiency in cold and ultracold ion–molecule interactions. In the presence of relativistic spin–orbit interactions, real crossings may transform into avoided crossings, which lies beyond the scope of this paper. These crossings, whether real or avoided, provide viable mechanisms for facilitating non-radiative and non-adiabatic charge transfer between ions and atoms in excited electronic configurations.

The PECs for the highly excited electronic states exhibit particularly fascinating behavior, characterized by pronounced undulations that include multiple barriers and potential wells. These intricate features are closely linked to the oscillatory nature of the atomic radial electron density in highly excited states, reflecting the underlying structure of the highly excited electronic orbitals. From the calculated adiabatic energies, values for the

minimum-to-minimum electronic excitation energy T_e, equilibrium internuclear distance R_e, dissociation energies (D_e), harmonic frequency ω_e, and rotational constant B_e have been calculated by the use of the least squares interpolation method for all bound states.

The obtained spectroscopic parameters of the corresponding molecular ions $MgRb^+$ and $SrRb^+$ are presented, respectively, with other previous experimental and theoretical results in Tables 3 and 4. For $MgRb^+$, our spectroscopic parameters of the ground state ($1^1\Sigma^+$) are R_e = 7.33 Bohr, D_e = 2352 cm^{-1}, ω_e = 84.19 cm^{-1}, $\omega_e x_e$ = 0.83 cm^{-1}, and B_e = 0.059151 cm^{-1}. These values are in excellent agreement with those presented by Tomza et al. [32] (R_e = 7.41 Bohr, D_e = 2237 cm^{-1}, ω_e = 84.1 cm^{-1}, and B_e = 0.058600 cm^{-1}). They used the CCSD(T) level of theory, ECP28MDF pseudopotentials for the Rb atom, and (aug-cc-pCVQZ) basis sets for the Mg atom. For the $MgRb^+$ molecular ion, only the ground electronic state has been previously investigated; all excited states presented in this work are reported here for the first time.

Table 3. Spectroscopic parameters of the ground and electronically excited states of $MgRb^+$ molecular ion.

State	R_e (Bohr)	D_e (cm^{-1})	T_e (cm^{-1})	ω_e (cm^{-1})	$\omega_e x_e$ (cm^{-1})	B_e (cm^{-1})	Reference
$X^1\Sigma$	7.33	2352	0	84.19	0.83	0.059151	This work
	7.41	2237	0	84.1		0.058600	[32]
$2^1\Sigma^+$	11.29	2182	28,285	45.96	0.18	0.024964	This work
$3^1\Sigma^+$	15.57	1454	36,296	28.22	0.08	0.013123	This work
$4^1\Sigma^+$	19.42	1416	41,787	21.82	0.06	0.008437	This work
$5^1\Sigma^+$	26.14	375	45,450	11.65	0.07	0.004656	This work
$1^1\Pi$	8.44	852	36,899	40.03	0.55	0.044675	This work
$2^1\Pi$	15.34	304	42,901	17.52	0.18	0.013519	This work
$3^1\Pi$	18.34	896	48,425	16.43	0.06	0.009462	This work
$1^1\Delta$ *	Repulsive						This work
$1^3\Sigma^+$	8.27	5198	19,166	80.35	0.30	0.046547	This work
$2^3\Sigma^+$	15.04	668	29,799	25.75	0.23	0.014060	This work
$3^3\Sigma^+$	16.68	2947	40,256	29.84	0.05	0.011440	This work
$4^3\Sigma^+$	29.05	192	43,313	7.74	0.08	0.003770	This work
$1^3\Pi$	7.51	535	23,830	55.84	1.32	0.056425	This work
$2^3\Pi$	13.62	599	42,606	23.53	0.16	0.017156	This work
$3^3\Pi$	18.78	1128	48,693	17.70	0.05	0.009024	This work
$1^3\Delta$ *	Repulsive						This work

* $1^1\Delta$ and $1^3\Delta$ are repulsive states.

The molecular ion $SrRb^+$ system was extensively studied in its ground state [21,32,42]; however, some excited states were represented only by Aymar et al. [42]. We compare our spectroscopic constants with the previously available theoretical results (see Table 4). Our calculation approach (FCI) is similar to that used in the paper of Aymar et al.; however, Tomza et al. [32] used the CCSD(T) level of theory. Despite our using two different theoretical approaches and methods to calculate the ground state interaction energy, the agreement between our results and those obtained by Tomza et al. [32] is very good (see Table 4). This good agreement is confirmed by the excellent accord between the well depths (4225/4247 cm^{-1}), as well as the equilibrium distance (8.24/8.34 Bohr). As can be seen in Table 4, the comparison with the results obtained by Aymar et al. [42] using the same approach also shows an excellent agreement. This good agreement is also obtained for the harmonic frequency ω_e. A similar accord, with the theoretical data obtained by Aymar et al. [42] for the remaining spectroscopic constants for the excited states, is also

observed. The higher-excited states $5^1\Sigma^+$, $3^1\Pi$, $4^3\Sigma^+$, and $3^3\Pi$ dissociating into $Sr^+(^2S(5s))$ + $Rb(^2P(5p))$ are represented here for the first time for $SrRb^+$.

Table 4. Spectroscopic parameters of the ground and electronically excited states of $SrRb^+$ molecular ion.

State	R_e (Bohr)	ΔR_e (%)	D_e (cm^{-1})	ΔD_e (%)	T_e (cm^{-1})	ω_e (cm^{-1})	$\Delta\omega_e$ (%)	$\omega_e x_e$ (cm^{-1})	B_e (cm^{-1})	Reference
$X^1\Sigma^+$	8.24		4225			58.09		0.18	0.020494	This work
	8.34	1.2	4247			59.00	1.6		0.020100	[32]
	8.23	0.1	4266	1.0		59.41	2.3		0.0205	[21]
	8.2	0.5	4285	1.4		58.00	0.2			[42]
$2^1\Sigma^+$	13.81		895		15,645	20.68		0.11	0.007297	This work
	13.79	0.1	933	4.2	15,752.3	20.94	1.3		0.0073	[21]
	13.8	0.1	960	7.3		21.00	1.5			[42]
$3^1\Sigma^+$	8.88		3143		21,933	46.60		0.12	0.017632	This work
	8.09	8.9	3122	0.7		47.00	0.9			[42]
2nd well	16.02		1216		23,861	16.47		0.055	0.001518	This work
	15.8	1.4	1132	6.9		16.00	2.9			[42]
$4^1\Sigma^+$	13.52		1000		24,557	37.19		0.49	0.007611	This work
	13.6	0.6	1012	1.2		31.00	16.6			[42]
$5^1\Sigma^+$	9.50		723 *							This work
	14.39		1231 *							This work
	21.64		933		28,342	12.18		0.45	0.015415	This work
$1^3\Sigma^+$	9.20		6474		10,068	49.57		0.09	0.016450	This work
	9.20		6544	1.1		49.00	1.2			[42]
$2^3\Sigma^+$	8.52		976 *							This work
	8.5	0.2	954	2.3		49.00				[42]
2nd well	17.98		881		17,863	14.99		0.16	0.019179	This work
	18.00	0.1	893	1.4		15.00	0.1			[42]
$3^3\Sigma^+$	11.26		1694		21,207	123.97		6.46	0.010977	This work
	11.00	2.3	1923	13.5						[42]
$4^3\Sigma^+$	19.39		1445		27,830	15.48		0.03	0.003701	This work
$1^1\Pi$	8.67		3563		21,515	43.66		0.08	0.018522	This work
	8.7	0.3	3561	0.1		44.00	0.8			[42]
$2^1\Pi$	8.71		2024		23,535	39.82		0.31	0.018340	This work
	8.7	0.1	2049	1.2		40.00	0.5			[42]
$3^1\Pi$	18.65		76		29,204	6.48		0.14	0.003999	This work
$1^3\Pi$	7.54		4229		14,518	63.72		0.20	0.024448	This work
	7.6	0.8	4240	0.3		64.00	0.4			[42]
$2^3\Pi$	9.04		2479		20,423	43.57		0.13	0.017045	This work
	9.0	0.4	2551	2.9		44.00	0.1			[42]
$3^3\Pi$	17.07		139		29,141	8.38		0.11	0.004775	This work
$1^1\Delta$	8.49		4551		20,527	51.11		0.11	0.019320	This work
	8.5	0.1	4533	0.4		52.00	1.6			[42]
$1^3\Delta$	8.6		3068		19,834	48.09		0.12	0.018818	This work
	8.6		3150	2.7		49.00	1.7			[42]

* Barrier.

A comparison of the spectroscopic constants reveals systematic differences between the $MgRb^+$ and $SrRb^+$ molecular ions. Notably, the equilibrium bond lengths (R_e) of $SrRb^+$ are generally longer than those of $MgRb^+$ for corresponding electronic states. For example, the ground state $X^1\Sigma^+$ has R_e = 7.33 Bohr for $MgRb^+$ and 8.24 Bohr for $SrRb^+$. This trend reflects the larger atomic radius and higher polarizability of the strontium atom compared to magnesium, which resulted in a shallower potential well and a more extended bond. Similarly, the electronic excitation energies (T_e) tend to be smaller for $SrRb^+$ than for $MgRb^+$ in the corresponding excited states. For instance, the $2^1\Sigma^+$ state has $T_e \approx 28{,}285$ cm^{-1} in $MgRb^+$ and ≈15645 cm^{-1} in $SrRb^+$. This is primarily due to the lower energy spacing

between the valence and excited states in Sr, stemming from its heavier mass and more diffuse electron cloud. Furthermore, the stronger long-range polarization interaction in $SrRb^+$, due to its higher dipole polarizability, also contributes to the lowering of the excited-state potential energy curves. These effects stem from intrinsic differences between the atomic structures of Mg and Sr. In addition, the Sr configuration possesses more diffuse outer orbitals and lower excitation energies compared to Mg, which has a more compact configuration. Indeed, these atomic-level distinctions significantly affect the molecular potential energy curves, equilibrium bond lengths, and associated spectroscopic constants.

3.2. Permanent and Transition Dipole Moments (PDMs and TDMs)

In addition, producing ultracold ions or dipolar molecules remains a current experimental challenge that demands precise knowledge of their electronic properties to effectively guide ongoing efforts. Within this framework, the dipole moment stands out as a key parameter, critically influencing the electric and optical behavior of molecules. Unlike potential energy curves, systematic calculations of permanent or transition dipole moments as functions of internuclear distance are relatively limited. To date, the only available data for the $SrRb^+$ molecular ion are those reported by Aymar et al. [42]. In our study, the PDMs are calculated with the origin positioned at the center of mass of the molecule. As a result, they exhibit a linear divergence at large internuclear distances, reflecting the increasing separation between the centers of negative and positive charge as the atoms and ions move farther apart. Figures 2 and 3 present the PDMs for the electronic states of $^{1,3}\Sigma^+$, $^{1,3}\Pi$, and $^{1,3}\Delta$ symmetries, respectively, for $MgRb^+$ and $SrRb^+$ molecular ions. At small internuclear distances, we observe that the PDMs of these electronic states show several abrupt changes. These changes correspond to avoided crossings between nearby electronic states and reflect sudden changes in the nature of the electronic wave functions. At large internuclear distances, the absolute values of the PDMs increase as the atoms move farther apart, eventually approaching a limit where the electric charge is fully localized on one of the atoms. The same behavior was previously observed for heteronuclear molecular ions [41,42]. In contrast to neutral molecules, the permanent dipole moments are effectively significant even when molecular ions are very weakly bound. At large internuclear distances, the permanent dipole moment of the states dissociating into AlkE + Rb^+ limits are positive. For the remaining states that dissociate into $AlkE^+$ + Rb, we observe a significant negative permanent dipole moment in a specific region. At large distances, these dipole moments show the same linear trend, indicating the growing separation between the centers of negative and positive charge.

The variation in the TDMs is also evaluated. We present only TDMs from $1^{1,3}\Sigma^+$ to $(i + 1)^{1,3}\Sigma^+$ (Figure 4) electronic states for both $MgRb^+$ and $SrRb^+$ ionic systems (i = 1, 2). The results obtained for $SrRb^+$ and those obtained in Ref. [42] of Aymar et al. have quite similar shapes and values, confirming the reliability of our calculation. The transition dipole moments for $MgRb^+$ are presented for the first time and have similar shapes to those obtained for $SrRb^+$. Generally, we notice that the variation in the adiabatic TDMs does not follow a well-defined law. We obtain a frequent and abrupt variation at the distance, which corresponds to an avoided crossing. The peaks of the TDMs, generally found at short distances, are large in the case where the crossings would be at least avoided and depending on the overlap between related states. At larger distances, the TDM tends toward a constant or zero, as for allowed or forbidden transitions. Indeed, the purely atomic transition corresponds to the atomic neutral–neutral type. Conversely, the dipole moment associated with the ionic–neutral transition vanishes due to the lack of overlap between the respective wave functions, as constrained by the dipole operator.

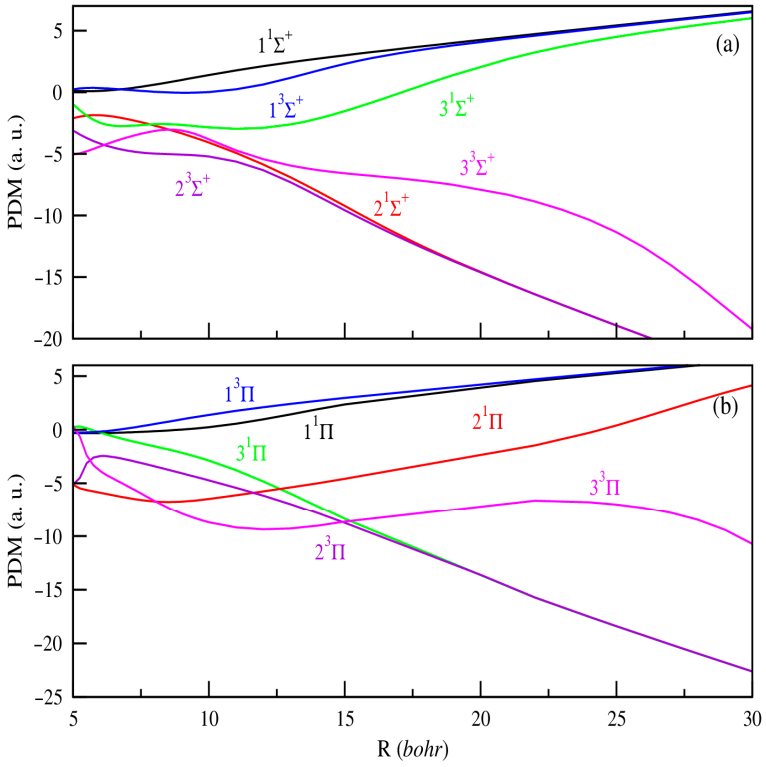


Figure 2. PDMs for the $^{1,3}\Sigma^+$(panel (**a**)) and $^{1,3}\Pi$, (panel (**b**)) electronic states of $MgRb^+$.

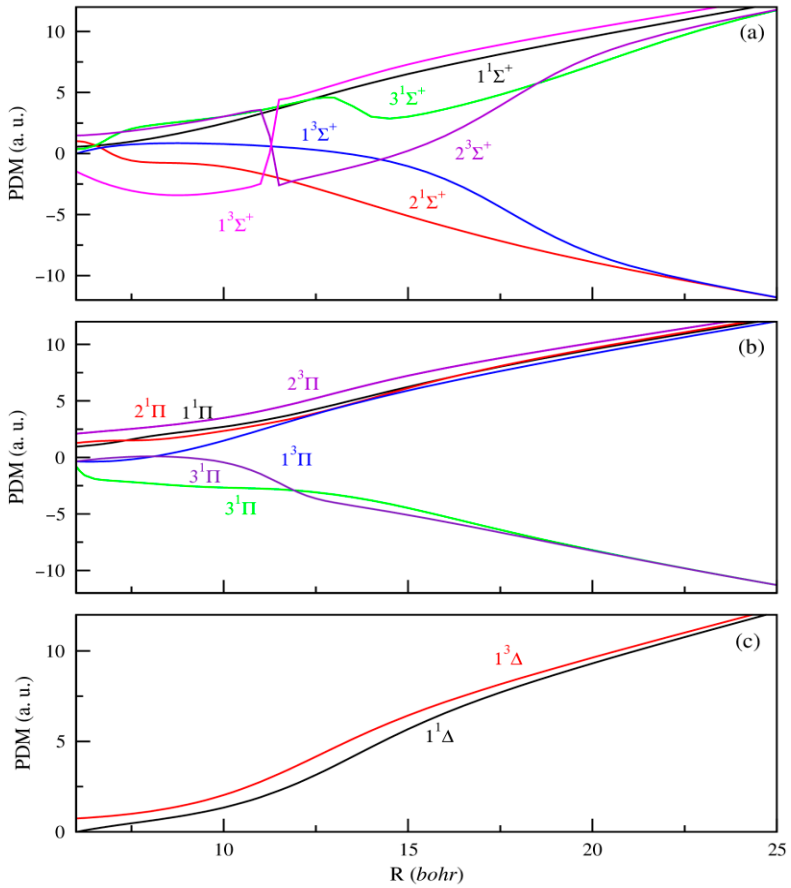


Figure 3. PDMs for the $^{1,3}\Sigma^+$ (panel (**a**)), $^{1,3}\Pi$, (panel (**b**)) and $^{1,3}\Delta$ (panel (**c**)) electronic states of $SrRb^+$.

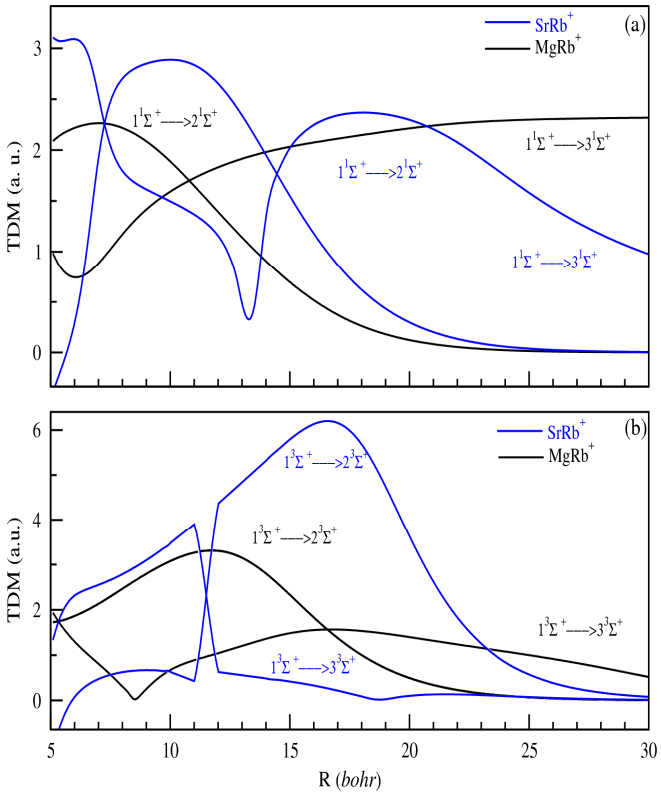


Figure 4. TDMs from $1^1\Sigma^+$ to $(i + 1)^1\Sigma^+$ (panel (**a**)) and $1^3\Sigma^+$ to $(i + 1)^3\Sigma^+$ (panel (**b**)) electronic states of $MgRb^+$ and $SrRb^+$ (i = 1, 2).

All the transitions between calculated electronic states of the same symmetry are also considered.

3.3. Exploitation of Results: Atom–Ion Elastic Scattering Proprieties, Vibrational Levels, Radiative Lifetimes, and the Possibility of Formation via Photoassociation

This section focuses on ion–atom elastic collisions at ultracold temperatures involving alkaline-earth-metal ions (Mg^+ and Sr^+) and the alkali atom Rb, occurring in the first excited electronic state, $2^1\Sigma^+$. The partial wave cross sections as functions of the collision energy (E) have been computed for the three lowest angular momentum states *s*-wave ($l = 0$), *p*-wave ($l = 1$), and *d*-wave ($l = 2$) for both $MgRb^+$ and $SrRb^+$ molecular systems. These results are illustrated in Figure 5.

For both systems, the partial wave cross section for the *s*-wave (l = 0) plays a dominant role even at very-low collision energies (i.e., $E \to 0$) while the other higher partial waves vary according to Wigner's threshold law. According to this law, as $k \to 0$, the phase shift for *l*-th partial waves goes as $\eta_l \sim k^{2l+1}$ for $l \leq (n-3)/2$, or otherwise $\eta_l \sim k^{n-2}$ for long-range potentials which behave like $\sim \frac{1}{r^n}$. As a result, in the low-energy limit $(k \to 0)$, the *s*-wave cross section becomes energy-independent, while the contributions from higher partial waves decrease proportionally to k^2. As the collision energy increases beyond the regime described by Wigner's threshold law, the *s*-wave cross section shows a distinct minimum at low energy. This behavior is associated with the Ramsauer–Townsend effect, where destructive interference in the scattering wave function leads to a temporary reduction in the scattering probability. Notably, at the Ramsauer minimum of *s*-wave scattering, both *p*-wave and *d*-wave elastic cross sections remain finite. This means that *p*- or *d*-wave interactions can be explored for ion–atom systems at the minimum position that occurs at a relatively low energy (μ-Kelvin and milli-Kelvin regime).

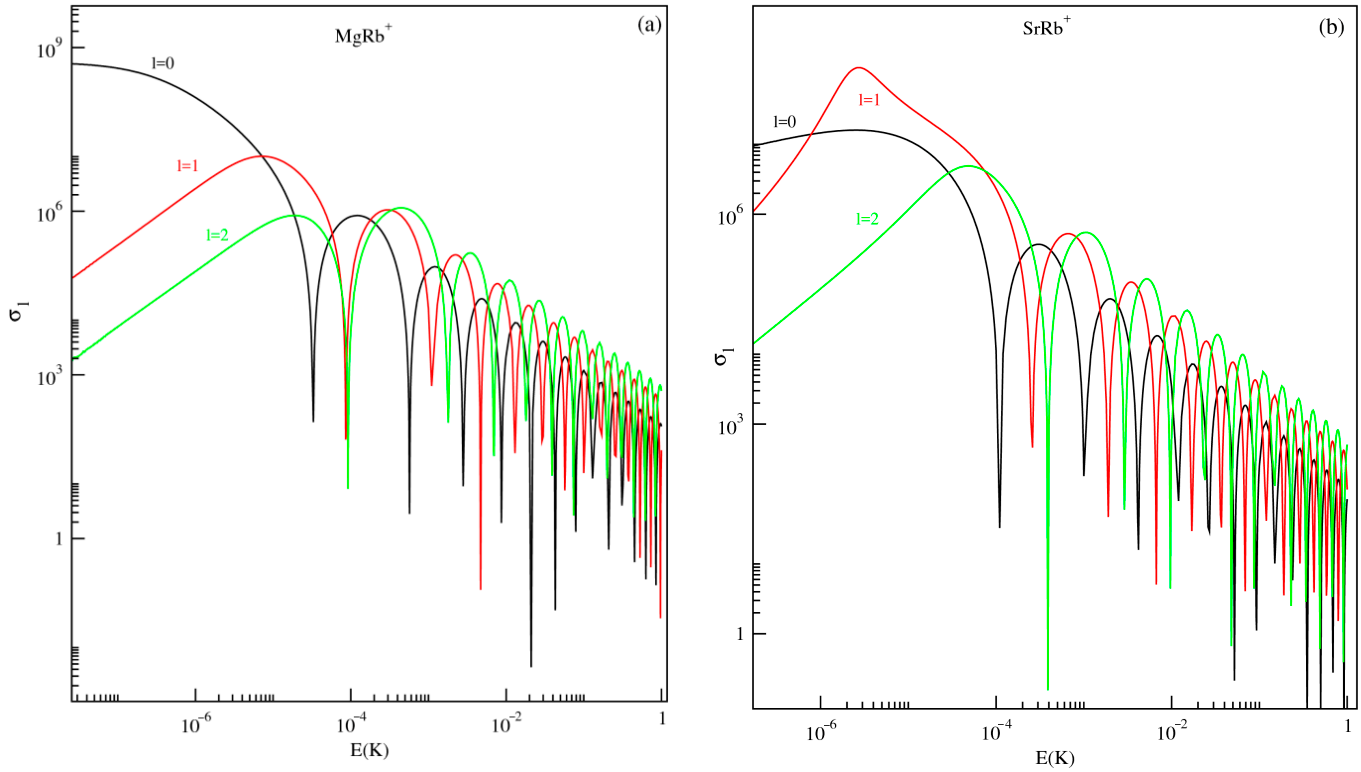


Figure 5. Partial wave scattering cross section as a function of collision energy E (in Kelvin) for the $MgRb^+$ (panel (**a**)) and $SrRb^+$ (panel (**b**)) molecular ions in the first excited state $2^1\Sigma^+$.

The total elastic scattering cross sections (σ_{tot}) are also calculated and they are plotted, as a function of collision energy E, where the collision is occurring in the first excited state $2^1\Sigma^+$, in Figure 6 for $MgRb^+$ and $SrRb^+$ molecular ions in panels (a) and (b), respectively. To achieve converged results at collision energies above 1 mK, it was necessary to include more than 85 partial waves. This is because, as the energy increases, a larger number of partial waves begin to contribute significantly to the total scattering cross section σ_{tot}. For a given energy E, a specific partial wave l will contribute meaningfully only if the height of its associated centrifugal barrier is not much greater than E. An estimate for the minimum number of partial waves required for convergence can be made by assuming that the centrifugal barrier height for the highest contributing partial wave is roughly one order of magnitude greater than the collision energy. This criterion ensures that all relevant partial waves are accounted for in the calculation. Figure 6 illustrates that in the ultra-low-energy region (below 1 μK), only the s-wave dominates the scattering process. When we consider the logarithm of both sides of Equation (9), a straight line is obtained having the form $log\sigma_{tot} = -\frac{1}{3}E + c_E$. The slope of the straight line should be $-1/3$ and the intercept c_E depends on the dipole polarizability coefficient (C_4) of the long-range part of the potential energy as defined in Equation (9). By the linear curve fitting of $log\sigma_{tot}$ vs. $logE$ of Figure 6a,b we find that the numerically calculated slope is quite close to the actual value $-1/3$. In addition, the calculation of c_E is quite close to that obtained by our numerical calculation.

In addition, the prediction of the formation of cold molecular systems also requires the knowledge of the vibrational lifetimes as well as absorption and emission spectra. In current experiments with cold ion–atom systems, vibrational lifetimes provide valuable insights into the formation mechanisms and spectroscopic behavior of molecular ions. In this part of the paper, we represent in Figure 7 the vibrational level spacing between the adjacent vibrational states (E_v–$E_{(v-1)}$) of the ground and bound excited electronic states $^{1,3}\Sigma^+$ of

the investigated $MgRb^+$ and $SrRb^+$ molecular ions, while radiative transition probabilities (Einstein coefficients) and the lifetimes for all vibrational levels of both ground $1^1\Sigma^+$ and first excited states $2^1\Sigma^+$ are illustrated in Figure 8, panels (a), (b), and (c), respectively.

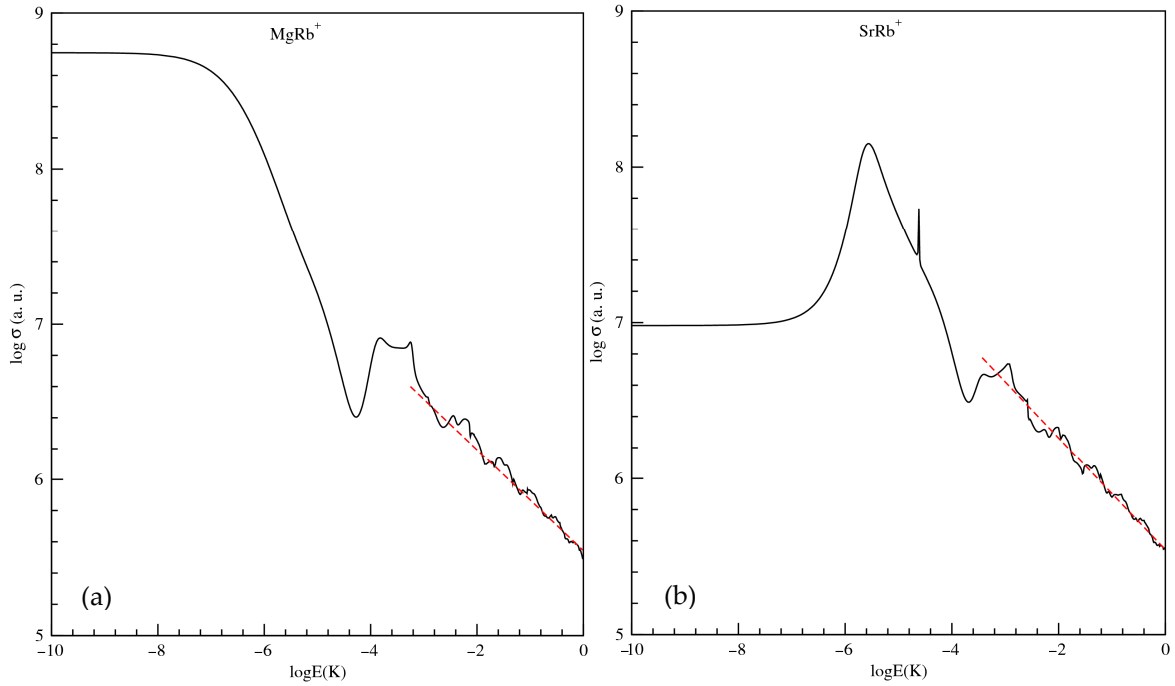


Figure 6. Total elastic scattering cross section as a function of collision energy E (in Kelvin) for the $MgRb^+$ (panel (**a**)) and $SrRb^+$ (panel (**b**)) molecular ions in the first excited state $2^1\Sigma^+$. Red dashed line represents the analytical high-energy asymptotic behavior of the cross section for long-range ion–neutral interactions, following a $\propto E^{-1/3}$ power law.

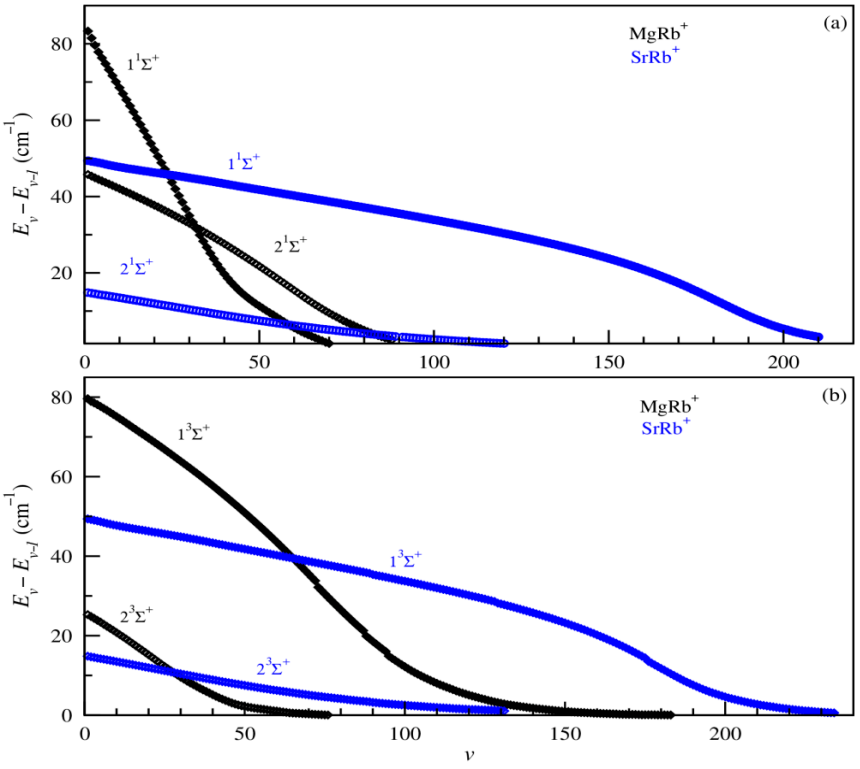


Figure 7. Vibrational energy level spacing for $^1\Sigma^+$ (panel (**a**)) and $^3\Sigma^+$ (panel (**b**)) electronic states of $MgRb^+$ and $SrRb^+$ molecular ions.

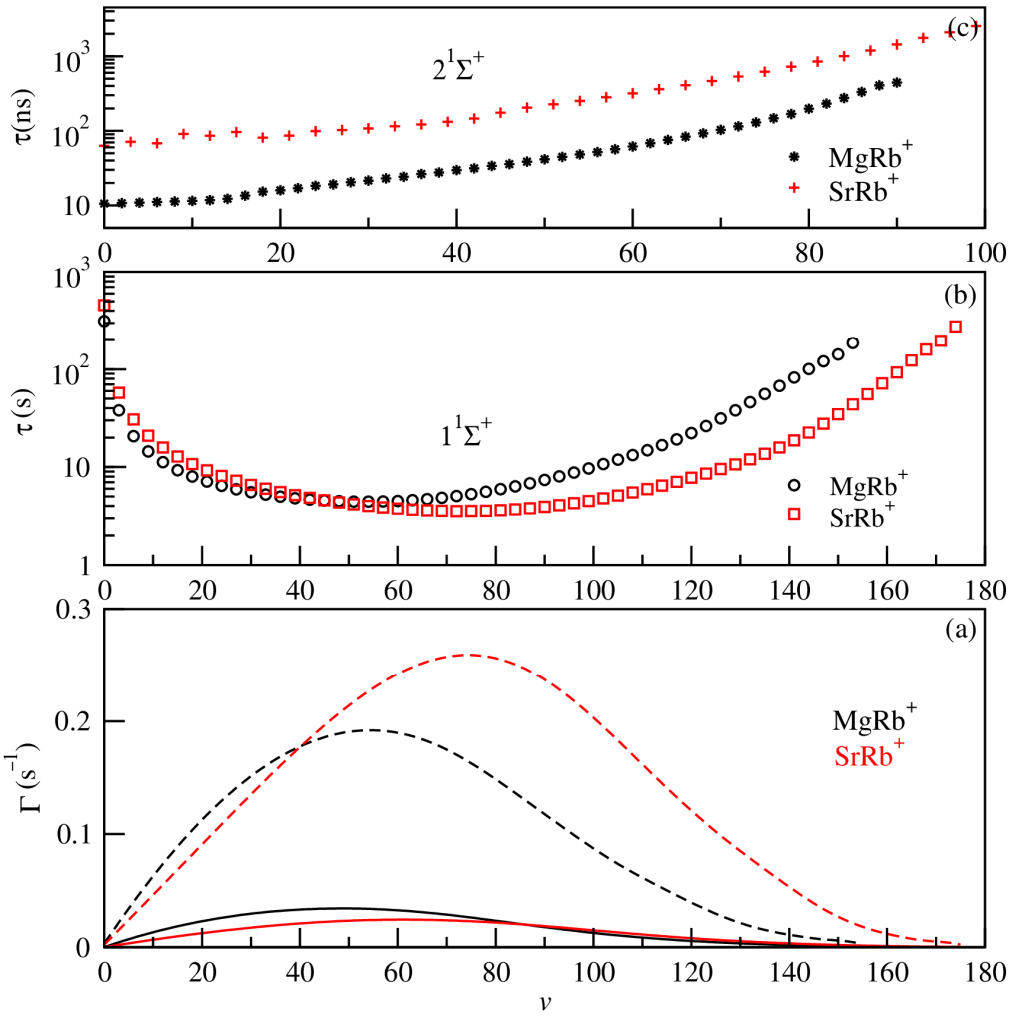


Figure 8. The spontaneous (full lines) and blackbody radiation-stimulated (dashed lines) transition rates for the vibrational levels of the ground $1^1\Sigma^+$ electronic state (panel (**a**)), lifetimes for vibrational levels of the ground $1^1\Sigma^+$ (panel (**b**)) state, and radiative lifetimes for the first excited state $2^1\Sigma^+$ (panel (**c**)) for both $SrRb^+$ (red) and $MgRb^+$ (black) ionic molecules.

We have analyzed the vibrational level energies for all electronic states of the $MgRb^+$ and $SrRb^+$ molecular ions by solving the radial Schrödinger equation using the computed adiabatic potential energy curves. The vibrational energies, calculated using the Numerov propagation method, were further refined through the Discrete Variable Representation (DVR) approach [51]. These vibrational properties offer deeper insight into the shape, depth, and structure of the potential wells associated with each electronic state. They also provide valuable information on the approximate term values and the positions of vibrational band heads.

As illustrated in Figure 7, the vibrational level spacings display a consistent trend, characteristic of ionic systems governed by long-range C_4/R^4 interactions. This extended asymptotic behavior leads to broad potential wells, enabling several electronic states to accommodate a high density of vibrational levels.

For the ground electronic state, there are 92 and 174 vibrational levels for the $MgRb^+$ and $SrRb^+$ molecular ions, respectively. The number of vibrational levels increases with the mass of the alkali-metal atom involved, even though the potential well depth decreases. This is because the effect of the increasing reduced mass outweighs the reduction in well depth. Additionally, the spacing between successive vibrational levels gradually decreases as the vibrational energy rises, highlighting the pronounced anharmonicity of

the potential energy curves (PECs). The anharmonic character of the $MgRb^+$ and $SrRb^+$ potentials is clearly observed. The vibrational level spacings are not uniform and gradually decrease with increasing vibrational quantum number v, eventually approaching zero at the dissociation limit. For the highly excited states with symmetry $^3\Sigma^+$, some sudden drops in vibrational energy levels are observed. These can be attributed to the widening of the potential well or the emergence of a secondary well, both of which significantly alter the vibrational structure of the state.

The overall pattern of energy spacing of different electronic states for the different molecular ions is similar. For the radiative lifetime calculations, for the ground $1^1\Sigma^+$ and first excited states $2^1\Sigma^+$, we exploited the obtained potential energy curves, permanent dipole moments, and transition dipole moments of the considered molecular ions. The magnitude of transition rates (see Figure 8a) for the vibrational levels depends on the permanent dipole moment and the overlap of wave functions of vibrational levels. For highly excited vibrational states, the transition frequency ω_{if} of the energy difference between levels i and f becomes very small due to the strong anharmonicity of the potential energy curve. Both the transition dipole moment and the transition frequency play key roles in determining the rates of spontaneous emission as well as blackbody radiation (BBR)-induced stimulated absorption and emission. As a result of these factors, the vibrational lifetime, when analyzed as a function of the vibrational quantum number v, shows a distinct pattern: it reaches a minimum at $v = 54$ for $MgRb^+$ and at $v = 73$ for $SrRb^+$. Beyond these points, the lifetime begins to increase again, eventually approaching or even exceeding the lifetime of the ground vibrational state ($v = 0$).

The shortest lifetime, observed at $\nu = 54$ for $MgRb^+$, corresponds to the peak of the stimulated transition rate and is also near the maximum of the spontaneous transition rate. This indicates a strong coupling between vibrational states at this level, leading to enhanced decay processes.

For higher vibrational levels, both spontaneous and stimulated rates gradually decrease. This is because the transition frequencies ω_{if} between the highly excited vibrational states become smaller, as these levels lie very close to one another in energy. As a result, the lifetimes of these states increase and may reach values comparable to, or even exceeding, the lifetime of the ground vibrational state. The radiative lifetime for $2^1\Sigma^+$ vibrational levels includes contributions from two types of transitions: bound–bound and bound–free. The bound–free component is calculated using the Franck–Condon approximation (for more details see our previous work, Refs. [22,52]). This approximation allows reproducing the radiative lifetime components for diatomic vibronic states and it has high efficiency for non-diagonal systems, particularly for those with significant continuum contributions. The radiative lifetime using this approximation is based on the wave function of the vibrational level belonging to the $2^1\Sigma^+$ excited electronic state. The radiative lifetimes of the first excited state $2^1\Sigma^+$ (presented in Figure 8c) increase with the increase of vibrational levels from nanoseconds to microseconds. The radiative lifetimes for the lowest vibrational level $v = 0$ are predicted to be 10.579 ns and 63.159 ns, respectively, for $MgRb^+$ and $SrRb^+$ systems.

4. Conclusions

This paper is a comprehensive and in-depth investigation of the molecular ions $MgRb^+$ and $SrRb^+$. A computation of PECs, corresponding spectroscopic parameters, and permanent and transition dipole moments for the ground and low-lying excited states of $^{1,3}\Sigma^+$, $^{1,3}\Pi$, and $^{1,3}\Delta$ symmetries have been carried out for both molecular systems. For Mg^{2+}, Sr^{2+}, and Rb^+ cores, a non-empirical pseudopotential approach is employed, which permits treating the molecule as a two-electron system. This simplification enables the use of full configuration interaction (FCI) calculations with relative ease. When the goal is to

precisely attain more excited states, this method takes advantage of large Gaussian basis sets. Our initial findings align well with earlier theoretical investigations of the ground and excited electronic states of the $SrRb^+$ molecular ion [21,32,42], as well as the ground state of $MgRb^+$ [32], indicating the precision of the utilized computational methodology. This is the first study on the structure of the excited electronic states of the $MgRb^+$ molecular ion.

The ab initio data have been used to determine the radiative lifetimes of the ground and first excited states of both molecules. The radiative lifetimes of the excited state $2^1\Sigma^+$ vibrational levels have an order of nanoseconds, while those of the ground state $1^1\Sigma^+$ vibrational levels are on the order of seconds. Furthermore, we have studied the elastic collision processes that can take place when cold Mg^+ or Sr^+ ions engage with Rb atoms. We calculated the low-energy elastic scattering parameters of the first excited state. We noticed that the 1/3 rule of scattering is observed at higher-energy regimes for both Rb-Mg^+ and Rb-Sr^+ ionic molecules, and that the Wigner threshold regime is achieved at the energy of micro-Kelvin collisions.

Author Contributions: Conceptualization, M.F., H.L., W.Z. and H.B.; methodology, M.F., H.L., W.Z. and H.B.; software, M.F., H.L. and W.Z.; validation, H.B., H.L. and W.Z.; writing—original draft preparation, M.F.; writing—review and editing, M.F., H.B., H.L. and W.Z.; visualization, M.F., H.L. and W.Z.; supervision, H.B.; project administration, H.B.; funding acquisition, H.B. All authors have read and agreed to the published version of the manuscript.

Funding: This research received no external funding.

Data Availability Statement: Requests for data on potential energy curves, as well as permanent and transition electric dipole moments as functions of interatomic distance, can be directed to the corresponding authors upon request.

Acknowledgments: H.B. would like to acknowledge the financial support of the American University of Ras Al Khaimah under the seed grant no. AAS/003/24.

Conflicts of Interest: The authors declare that they have no conflicts of interest relevant to this study.

References

1. Tomza, M.; Jachymski, K.; Gerritsma, R.; Negretti, A.; Calarco, T.; Idziaszek, Z.; Julienne, P.S. Cold hybrid ion-atom systems. *Rev. Mod. Phys.* **2019**, *91*, 035001. [CrossRef]
2. Tscherbul, T.V.; Brumer, P.; Buchachenko, A.A. Spin-orbit interactions and quantum spin dynamics in cold ion-atom collisions. *Phys. Rev. Lett.* **2016**, *117*, 143201. [PubMed]
3. Willitsch, S. Ion-atom hybrid systems. In *Ion Traps for Tomorrow's Applications*; IOS Press: Amsterdam, The Netherlands, 2015; pp. 255–268.
4. Eberle, P.; Dörfler, A.D.; von Planta, C.; Ravi, K.; Haas, D.; Zhang, D.; van de Meerakker, S.Y.T.; Willitsch, S. Ion-atom and ion-molecule hybrid systems: Ion-neutral chemistry at ultralow energies. *J. Phys. Conf. Ser.* **2015**, *635*, 012012.
5. Eberle, P.; Dörfler, A.D.; von Planta, C.; Ravi, K.; Willitsch, S. A Dynamic Ion–Atom Hybrid Trap for High-Resolution Cold-Collision Studies. *ChemPhysChem* **2016**, *17*, 3769–3775. [CrossRef]
6. Pérez Ríos, J. Cold chemical reactions between molecular ions and neutral atoms. In *An Introduction to Cold and Ultracold Chemistry: Atoms Molecules Ions and Rydbergs*; Springer: Berlin/Heidelberg, Germany, 2020; pp. 215–233.
7. Côté, R.; Dalgarno, A. Ultracold atom-ion collisions. *Phys. Rev. A* **2000**, *62*, 012709. [CrossRef]
8. Zipkes, C.; Palzer, S.; Ratschbacher, L.; Sias, C.; Köhl, M. Cold heteronuclear atom-ion collisions. *Phys. Rev. Lett.* **2010**, *105*, 133201. [CrossRef]
9. Ravi, K.; Lee, S.; Sharma, A.; Werth, G.; Rangwala, S.A. Cooling and stabilization by collisions in a mixed ion–atom system. *Nat. Commun.* **2012**, *3*, 1–7. [CrossRef]
10. Png, W.H.; Hsu, T.; Liu, T.W.; Lin, G.D.; Chang, M.S. Quantum computing with trapped ions: An overview. *IEEE Nanotechnol. Mag.* **2022**, *16*, 30–36. [CrossRef]
11. Doerk, H.; Idziaszek, Z.; Calarco, T. Atom-ion quantum gate. *Phys. Rev. A—At. Mol. Opt. Phys.* **2010**, *81*, 012708.
12. Perego, E.; Duca, L.; Sias, C. Electro-optical ion trap for experiments with atom-ion quantum hybrid systems. *Appl. Sci.* **2020**, *10*, 2222. [CrossRef]

13. Thielemann, F.; Siemund, J.; von Schoenfeld, D.; Wu, W.; Weckesser, P.; Jachymski, K.; Walker, T.; Schaetz, T. Exploring atom-ion Feshbach resonances below the s-wave limit. *Phys. Rev. X* **2025**, *15*, 011051.
14. Weckesser, P.; Thielemann, F.; Wiater, D.; Wojciechowska, A.; Karpa, L.; Jachymski, K.; Tomza, M.; Walker, T.; Schaetz, T. Observation of Feshbach resonances between a single ion and ultracold atoms. *Nature* **2021**, *600*, 429–433. [CrossRef]
15. Xing, X.; Weckesser, P.; Thielemann, F.; Jónás, T.; Vexiau, R.; Bouloufa-Maafa, N.; Luc-Koenig, E.; Madison, K.W.; Orbán, A.; Xie, T.; et al. Competing excitation quenching and charge exchange in ultracold Li-Ba+ collisions. *J. Phys. B At. Mol. Opt. Phys.* **2024**, *57*, 245201.
16. Takahashi, Y. Quantum simulation of quantum many-body systems with ultracold two-electron atoms in an optical lattice. *Proc. Jpn. Acad. Ser. B* **2022**, *98*, 141–160.
17. Côté, R. Ultracold hybrid atom–ion systems. In *Advances in Atomic, Molecular, and Optical Physics*; Academic Press: Cambridge, MA, USA, 2016; Volume 65, pp. 67–126.
18. Ladjimi, H.; Zrafi, W.; Farjallah, M.; Bejaoui, M.; Berriche, H. Electronic structure, cold ion–atom elastic collision properties and possibility of laser cooling of BeCs+ molecular ion. *Phys. Chem. Chem. Phys.* **2022**, *24*, 18511–18522. [PubMed]
19. Mahdian, A. Elastic and Inelastic Collisions in an Atom-Ion Experiment. Ph.D. Thesis, Universität Ulm, Ulm, Germany, 2023.
20. Gacesa, M.; Montgomery, J.A., Jr.; Michels, H.H.; Côté, R. Production of NaCa+ molecular ions in the ground state from cold atom-ion mixtures by photoassociation via an intermediate state. *Phys. Rev. A* **2016**, *94*, 013407.
21. da Silva, H., Jr.; Raoult, M.; Aymar, M.; Dulieu, O. Formation of molecular ions by radiative association of cold trapped atoms and ions. *New J. Phys.* **2015**, *17*, 045015. [CrossRef]
22. Ladjimi, H.; Sardar, D.; Farjallah, M.; Alharzali, N.; Naskar, S.; Mlika, R.; Berriche, H.; Deb, B. Spectroscopic properties of the molecular ions BeX+ (X = Na, K, Rb): Forming cold molecular ions from an ion–atom mixture by stimulated Raman adiabatic process. *Mol. Phys.* **2018**, *116*, 1812–1826. [CrossRef]
23. Sardar, D.; Naskar, S.; Pal, A.; Berriche, H.; Deb, B. Formation of a molecular ion by photoassociative Raman processes. *J. Phys. B At. Mol. Opt. Phys.* **2016**, *49*, 245202. [CrossRef]
24. Mølhave, K.; Drewsen, M. Formation of translationally cold MgH+ and MgD+ molecules in an ion trap. *Phys. Rev. A* **2000**, *62*, 011401. [CrossRef]
25. Staanum, P.F.; Højbjerre, K.; Wester, R.; Drewsen, M. Probing isotope effects in chemical reactions using single ions. *Phys. Rev. Lett.* **2008**, *100*, 243003. [CrossRef]
26. Bertelsen, A.; Vogelius, I.S.; Jørgensen, S.; Kosloff, R.; Drewsen, M. Photo-dissociation of Cold MgH ions: Towards rotational temperature measurements and controlled dissociation. *Eur. Phys. J. D-At. Mol. Opt. Plasma Phys.* **2004**, *31*, 403–408.
27. Jørgensen, S.; Drewsen, M.; Kosloff, R. Intensity and wavelength control of a single molecule reaction: Simulation of photodissociation of cold-trapped MgH+. *J. Chem. Phys.* **2005**, *123*, 94302. [CrossRef] [PubMed]
28. Aymar, M.; Dulieu, O. The electronic structure of the alkaline-earth-atom (Ca, Sr, Ba) hydride molecular ions. *J. Phys. B At. Mol. Opt. Phys.* **2012**, *45*, 215103. [CrossRef]
29. Belayouni, S.; Ghanmi, C.; Berriche, H. Adiabatic and quasi-diabatic investigation of the strontium hydride cation SrH+: Structure, spectroscopy, and dipole moments. *Can. J. Phys.* **2016**, *94*, 791–802. [CrossRef]
30. Shi, D.; Liu, X.; Shan, S.; Xu, H.; Yan, B. Configuration interaction study on the low-lying electronic states of strontium hydride cation including spin-orbit coupling. *Spectrochim. Acta Part A Mol. Biomol. Spectrosc.* **2017**, *180*, 29–36. [CrossRef]
31. Allouche, A.R.; Spiegelmann, F.; Aubert-Frécon, M. Theoretical study of the low-lying electronic states of the BaH+ molecular ion. *Chem. Phys. Lett.* **1993**, *204*, 343–349.
32. Śmiałkowski, M.; Tomza, M. Interactions and chemical reactions in ionic alkali-metal and alkaline-earth-metal diatomic AB+ and triatomic A 2 B+ systems. *Phys. Rev. A* **2020**, *101*, 012501.
33. Hall, F.H.; Eberle, P.; Hegi, G.; Raoult, M.; Aymar, M.; Dulieu, O.; Willitsch, S. Ion-neutral chemistry at ultralow energies: Dynamics of reactive collisions between laser-cooled Ca+ ions and Rb atoms in an ion-atom hybrid trap. *Mol. Phys.* **2013**, *111*, 2020–2032. [CrossRef]
34. Ben-shlomi, R.; Pinkas, M.; Meir, Z.; Sikorsky, T.; Katz, O.; Akerman, N.; Ozeri, R. High-energy-resolution measurements of an ultracold-atom–ion collisional cross section. *Phys. Rev. A* **2021**, *103*, 032805.
35. Smith, W.W.; Goodman, D.S.; Sivarajah, I.; Wells, J.E.; Banerjee, S.; Côté, R.; Michels, H.H.; Mongtomery, J.A.; Narducci, F.A. Experiments with an ion-neutral hybrid trap: Cold charge-exchange collisions. *Appl. Phys. B* **2014**, *114*, 75–80.
36. Meir, Z.; Sikorsky, T.; Ben-Shlomi, R.; Akerman, N.; Dallal, Y.; Ozeri, R. Dynamics of a ground-state cooled ion colliding with ultracold atoms. *Phys. Rev. Lett.* **2016**, *117*, 243401. [CrossRef]
37. Zipkes, C.; Palzer, S.; Sias, C.; Köhl, M. A trapped single ion inside a Bose–Einstein condensate. *Nature* **2010**, *464*, 388–391. [CrossRef]
38. Hall, F.H.; Aymar, M.; Raoult, M.; Dulieu, O.; Willitsch, S. Light-assisted cold chemical reactions of barium ions with rubidium atoms. *Mol. Phys.* **2013**, *111*, 1683–1690. [CrossRef]

39. ElOualhazi, R.; Berriche, H. Electronic structure and spectra of the MgLi+ ionic molecule. *J. Phys. Chem. A* **2016**, *120*, 452–465. [CrossRef] [PubMed]
40. Akkari, S.; Zrafi, W.; Ladjimi, H.; Bejaoui, M.; Dhiflaoui, J.; Berriche, H. Electronic structure of ground and low-lying excited states of BaLi+ molecular ion: Spin-orbit effect, radiative lifetimes and Franck-Condon factor. *Phys. Scr.* **2024**, *99*, 035403. [CrossRef]
41. Zrafi, W.; Ladjimi, H.; Said, H.; Berriche, H.; Tomza, M. Ab initio electronic structure and prospects for the formation of ultracold calcium–alkali-metal-atom molecular ions. *New J. Phys.* **2020**, *22*, 073015.
42. Aymar, M.; Guérout, R.; Dulieu, O. Structure of the alkali-metal-atom+ strontium molecular ions: Towards photoassociation and formation of cold molecular ions. *J. Chem. Phys.* **2011**, *135*, 6. [CrossRef]
43. Fuentealba, P.; Reyes, O. Pseudopotential calculations on the ground state of the alkaline-earth monohydride ions. *Mol. Phys.* **1987**, *62*, 1291–1296. [CrossRef]
44. Foucrault, M.; Millié, P.; Daudey, J.P. Nonperturbative method for core–valence correlation in pseudopotential calculations: Application to the Rb2 and Cs2 molecules. *J. Chem. Phys.* **1992**, *96*, 1257–1264. [CrossRef]
45. Ralchenko, Y.; Jou, F.C.; Kelleher, D.E.; Kramida, A.E.; Musgrove, A.; Reader, J.; Olsen, K. *NIST Atomic Spectra Database (Version 3.0.1)*; National Institute of Standards and Technology: Gaithersburg, MD, USA, 2006. Available online: https://webbook.nist.gov/chemistry/ (accessed on 3 May 2025).
46. Aymar, M.; Guérout, R.; Sahlaoui, M.; Dulieu, O. Electronic structure of the magnesium hydride molecular ion. *J. Phys. B At. Mol. Opt. Phys.* **2009**, *42*, 154025. [CrossRef]
47. Kaupp, M.; Schleyer, P.V.R.; Stoll, H.; Preuss, H. Pseudopotential approaches to Ca, Sr, and Ba hydrides. Why are some alkaline earth MX2 compounds bent? *J. Chem. Phys.* **1991**, *94*, 1360–1366. [CrossRef]
48. Zrafi, W.; Hela, L.; Berriche, H. Accurate ab initio calculations of adiabatic energy and dipole moment: Prospects for the formation of cold Alkaline-Earth-Francium molecular ions ALKE-Fr+ (ALKE = Be, Mg, Ca, and Sr). *Phys. Scr.* **2023**, *98*, 125403. [CrossRef]
49. Schwerdtfeger, P.; Nagle, J.K. 2018 Table of static dipole polarizabilities of the neutral elements in the periodic table. *Mol. Phys.* **2019**, *117*, 1200–1225.
50. Cooley, J.W. An improved eigenvalue corrector formula for solving the Schrödinger equation for central fields. *Math. Comput.* **1961**, *15*, 363–374.
51. Schweizer, W. Discrete Variable Method. In *Numerical Quantum Dynamics*; Springer: Berlin/Heidelberg, Germany, 2002; pp. 155–207. [CrossRef]
52. Zemke, W.T.; Crooks, J.B.; Stwalley, W.C. Radiative and nonradiative lifetimes for vibrational levels of the A 1Σ+ state of 7LiH. *J. Chem. Phys.* **1978**, *68*, 4628–4630. [CrossRef]

Disclaimer/Publisher's Note: The statements, opinions and data contained in all publications are solely those of the individual author(s) and contributor(s) and not of MDPI and/or the editor(s). MDPI and/or the editor(s) disclaim responsibility for any injury to people or property resulting from any ideas, methods, instructions or products referred to in the content.